
This is an electronic reprint of the original article.
This reprint *may differ* from the original in pagination and typographic detail.

Author(s): Lee, Wonjae; Gheorghe, Andrei H.; Tiurev, Konstantin; Ollikainen, Tuomas; Möttönen, Mikko; Hall, David S.

Title: Synthetic electromagnetic knot in a three-dimensional skyrmion

Year: 2018

Version:

Please cite the original version:

Lee, W., Gheorghe, A. H., Tiurev, K., Ollikainen, T., Möttönen, M., & Hall, D. S. (2018). Synthetic electromagnetic knot in a three-dimensional skyrmion. *Science Advances*, 4(3), Article eaao3820. <https://doi.org/10.1126/sciadv.aao3820>

All material supplied via JYX is protected by copyright and other intellectual property rights, and duplication or sale of all or part of any of the repository collections is not permitted, except that material may be duplicated by you for your research use or educational purposes in electronic or print form. You must obtain permission for any other use. Electronic or print copies may not be offered, whether for sale or otherwise to anyone who is not an authorised user.

PHYSICS

Synthetic electromagnetic knot in a three-dimensional skyrmion

Wonjae Lee,^{1*} Andrei H. Gheorghe,^{1†} Konstantin Tiurev,² Tuomas Ollikainen,² Mikko Möttönen,^{2,3} David S. Hall^{1‡}

Classical electromagnetism and quantum mechanics are both central to the modern understanding of the physical world and its ongoing technological development. Quantum simulations of electromagnetic forces have the potential to provide information about materials and systems that do not have conveniently solvable theoretical descriptions, such as those related to quantum Hall physics, or that have not been physically observed, such as magnetic monopoles. However, quantum simulations that simultaneously implement all of the principal features of classical electromagnetism have thus far proved elusive. We experimentally realize a simulation in which a charged quantum particle interacts with the knotted electromagnetic fields peculiar to a topological model of ball lightning. These phenomena are induced by precise spatiotemporal control of the spin field of an atomic Bose-Einstein condensate, simultaneously creating a Shankar skyrmion—a topological excitation that was theoretically predicted four decades ago but never before observed experimentally. Our results reveal the versatile capabilities of synthetic electromagnetism and provide the first experimental images of topological three-dimensional skyrmions in a quantum system.

INTRODUCTION

Ball lightning is a rare and little-understood phenomenon, commonly thought to be a localized, traveling electrical discharge with a lifetime significantly exceeding that of ordinary lightning (1). A topological theory of ball lightning (2, 3) ascribes this surprising persistence to the presence of an electromagnetic knot, with magnetic field lines consisting of closed, linked rings that support tangled electric currents in a plasma of ionized air. This knotted electromagnetic field structure is topologically protected because the field lines cannot be unlinked by continuous deformations, much as a Möbius strip cannot be converted to an untwisted band without cutting it.

Here, we report the remarkable observation that a close analog of this electromagnetic knot appears in the presence of a topological quantum-mechanical spin texture known as a Shankar skyrmion (4, 5). Originally considered in the context of field theories in particle physics (6), skyrmions are continuous topological excitations that are of great theoretical and experimental interest in diverse condensed-matter systems such as crystalline liquids (7), magnetic materials (8, 9), and superfluids (4, 5, 10–13). We create and image the first instance of this three-dimensional skyrmion using experimental techniques originally developed to create topological defects such as monopoles (14, 15) and knot solitons (16–19) in superfluid Bose-Einstein condensates (BECs).

The connection between the skyrmionic spin texture and the electromagnetic knot emerges in the context of synthetic electromagnetism (20, 21), a fascinating topic of growing importance to the field of quantum simulation (22). It is well known that electromagnetic effects arise in quantum mechanics in the form of gauge potentials that appear in the particle Hamiltonian. Analogous potentials can arise dynamically for

neutral ultracold atoms due to transformations to rotating or shaking reference frames or geometrically through spatiotemporal dependence of the internal degrees of freedom, such as those induced by atom-light interactions (20, 21). Under these conditions, the atomic wave function evolves as would that of a charged particle under the influence of the gauge potentials. Several experimental techniques now realize these potentials and their associated synthetic electric (23) or synthetic magnetic (24, 25) fields, permitting the recent experimental explorations of quantum Hall physics (26, 27), spin-orbit coupling (28), and the spin Hall effect (29) in ultracold atoms.

Curiously, classical electromagnetism itself may enter quantum mechanics in terms of potentials derived from the spatiotemporal variations of a nonintegrable phase factor multiplying the charged particle wave function (30, 31). An analogous situation occurs in ferromagnetic spin-1 BECs, where the local Berry phase arising from the spatiotemporal variations of the spin establishes synthetic gauge potentials for the scalar wave function (32). We take advantage of this correspondence by studying the synthetic fields and sources of the topological model of ball lightning (2, 3) created by a precise tailoring of the spin field.

RESULTS

Skyrmion creation

We begin with a description of the Shankar skyrmion and its experimental creation (Figs. 1 to 3) and subsequently turn to its synthetic electromagnetic properties (Figs. 1 and 4). The skyrmionic spin texture may be represented by a field of rigid triads, each oriented by specifying its spin axis and a rotation angle about it, in the manner shown in Fig. 1C. The skyrmion is a finite-sized object bounded by a background region of uniformly oriented triads, with a core that is identified as the locus of points with fully inverted spins. There are no singularities or discontinuities in the triad orientation, which changes smoothly and continuously as one travels along any path within the bounded region.

Let us consider this fascinating texture in detail. With regard to the spin axis of the triad, we note that all spin orientations may be found within the bounded region and that the sets of points in space sharing

Copyright © 2018
The Authors, some
rights reserved;
exclusive licensee
American Association
for the Advancement
of Science. No claim to
original U.S. Government
Works. Distributed
under a Creative
Commons Attribution
NonCommercial
License 4.0 (CC BY-NC).

¹Department of Physics and Astronomy, Amherst College, Amherst, MA 01002–5000, USA. ²QCD Labs, Academy of Finland Centre of Excellence in Computational Nanoscience, Department of Applied Physics, Aalto University, P.O. Box 13500, FI-00076 Aalto, Finland. ³University of Jyväskylä, Department of Mathematical Information Technology, P.O. Box 35, FI-40014 Jyväskylä, Finland.

*Present address: Department of Physics, Princeton University, Princeton, NJ 08540, USA.

†Present address: Department of Physics, Harvard University, Cambridge, MA 02138, USA.

‡Corresponding author. Email: dshall@amherst.edu

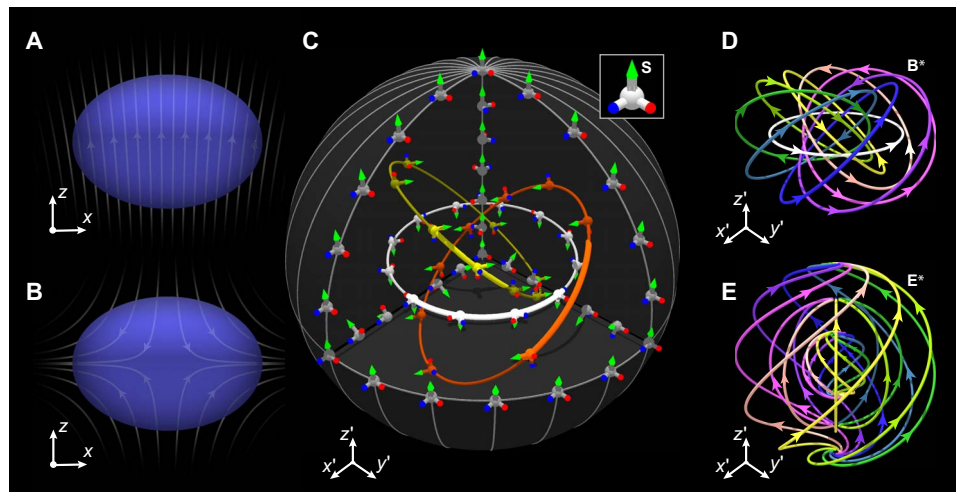


Fig. 1. Creation of the Shankar skyrmion and its synthetic electromagnetic fields. (A and B) External magnetic field (white field lines) applied to the condensate (blue ellipsoid) just before (A) and after (B) the commencement of the creation process. The field has a continuous rotational symmetry about the z axis. The spin vectors are initially aligned with the magnetic field depicted in (A) but are reoriented as they precess about the new field lines (B) at their local Larmor frequency. (C) Cutaway octant of the created Shankar skyrmion texture exhibiting its continuous and topologically nontrivial triad texture. The inset shows a triad, for which the local spin direction \mathbf{S} is marked by a green-tipped arrow. The blue- and red-tipped arms define the rotation angle of the triad about its spin vector. The colored curves are example contours, for which the spin vector points in a common direction, and along which the rotation angle winds about the direction of the spin by 4π . (D and E) Examples of the synthetic magnetic (D) and electric (E) field lines arising from the spin texture in (C), for which the colors are to guide the eye.

any particular spin orientation constitute closed curves, as illustrated in Fig. 1C. These curves are the fibers of the famous Hopf fibration (33), describing a knotted spin texture for which each fiber is linked with every other exactly once. Although this topological structure is reminiscent of that of the director field $\hat{\mathbf{d}}(\mathbf{r})$ in the recently observed quantum knot (19), the skyrmion is distinguished by an additional 4π twist in the triad orientation about its spin axis as one traverses a fiber. The triads thus smoothly pass through all possible orientations exactly twice within the skyrmion. Quantum knots, on the other hand, are described by a field of unit vectors and cannot express the topologically important twisting of the triad.

The skyrmionic spin texture is created experimentally within an optically trapped and spin-polarized ferromagnetic ^{87}Rb BEC (see Materials and Methods) that is exposed to an externally controlled magnetic field, described by

$$\mathbf{B}(\mathbf{r}', t) = \mathbf{B}_q(x', y', z') + \mathbf{B}_b(t) \quad (1)$$

where the condensate is taken to be at the origin of the rescaled coordinate system $x' = x$, $y' = y$, and $z' = 2z$. The term $\mathbf{B}_q = (x'\hat{x}' + y'\hat{y}' - z'\hat{z}')b_q$ is a quadrupole magnetic field of constant strength b_q , and \mathbf{B}_b is an additional time-dependent uniform magnetic field. For $t < 0$, $\mathbf{B}_b = B_b\hat{z}'$ is sufficiently strong that the magnetic field is essentially aligned with the z axis at the condensate (Fig. 1A and Materials and Methods). At $t = 0$, B_b is rapidly reduced to zero, ideally preserving the initial spin texture as it centers the magnetic field zero on the condensate (Fig. 1B). This nonadiabatic ramp initiates the skyrmion creation process as the spins precess in the inhomogeneous magnetic field \mathbf{B}_q . The skyrmion winding described above is complete after a full spin rotation at the radial boundary of the condensate. The rotation of the triad about the local spin can also be interpreted as the accumulation of nonadiabatic geometric phase, known as the Aharonov-Anandan phase (34), during the creation process. Note that the quantum knot experiment

of Hall *et al.* (19) involves the polar phase of ^{87}Rb and does not accumulate this geometric phase under similar experimental conditions.

Mean-field simulations of the experimental creation process, which do not include any free parameters, reveal the resulting skyrmion texture. For a quantization axis along z , the simulations show that the $m = +1$ spinor component dominates at the boundary of the condensate and near the z axis, the $m = -1$ component at the skyrmion core, and the $m = 0$ component in the intermediate toroidal region (Fig. 2, A and B). These qualitative features also appear in the analytically obtained texture in Fig. 1C.

We investigate the skyrmion texture experimentally after releasing the condensate from its confining potential, imaging the condensate density profiles in each of the three spinor components with a quantization axis chosen by a sudden ramp of the magnetic field (see Materials and Methods). The images for a spin quantization axis along z are shown in Fig. 2 (E and F) and are compared with those of the corresponding simulations that include the additional experimental steps, Fig. 2 (C and D). As the images indicate, the release from the trap, in conjunction with the nonzero superfluid velocity and initially inhomogeneous magnetic fields, deforms the density profiles significantly during the expansion. Nevertheless, the good agreement between the experimental and numerically calculated post-expansion images strongly supports the successful creation and observation of the skyrmion.

We also examine the spinor components in bases quantized along x and y (Fig. 3). These density profiles are sensitive to the quantum-mechanical phase coherence between the components in the original (z) basis, revealing that the full information about the texture goes beyond the density profiles shown in Fig. 2. The agreement between the experiments and the simulations is striking, embracing many of the smallest resolvable density features. Measurements of the temporal evolution with all three quantization axes are also in good agreement with the simulations (figs. S3, S4, and S5). Thus, we conclude that we have experimentally created a Shankar skyrmion in the condensate.

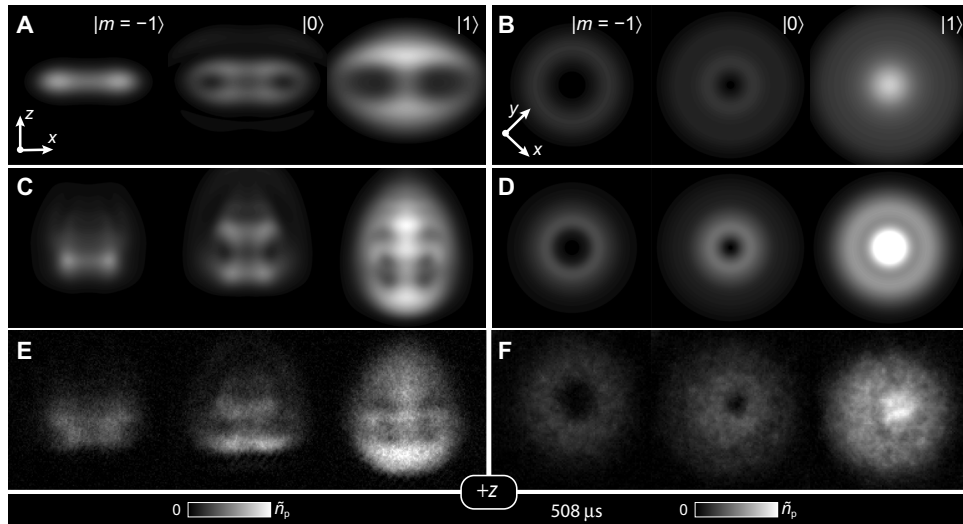


Fig. 2. Comparison of experiment with theory. Side (A) and top (B) column particle densities of the three spin states in the trap 508 μs after the nonadiabatic ramp, calculated using the experimental parameters (see Materials and Methods). (C to F) Calculated (C and D) and experimentally measured (E and F) post-expansion density profiles for an in-trap evolution time of 508 μs . The quantization axis is along +z. Throughout, the particle number is 2×10^5 . For (A) and (B), the field of view is $39 \mu\text{m} \times 13 \mu\text{m}$, and the maximum pixel intensity corresponds to column densities in excess of $\bar{n}_p = 3.8 \times 10^{11} \text{ cm}^{-2}$. For (C) and (E), these quantities are $738 \mu\text{m} \times 246 \mu\text{m}$ and $\bar{n}_p = 8.5 \times 10^8 \text{ cm}^{-2}$, and for (D) and (F), these quantities are $657 \mu\text{m} \times 219 \mu\text{m}$ and $\bar{n}_p = 1.0 \times 10^9 \text{ cm}^{-2}$, respectively.

Synthetic electromagnetic fields

Next, we study the synthetic electromagnetic fields arising from the spin texture of the Shankar skyrmion and demonstrate the presence of the knot. We use the conventional mean-field description of a BEC in terms of the spinor order parameter

$$\Psi(\mathbf{r}, t) = \psi(\mathbf{r}, t)\zeta(\mathbf{r}, t) = \sqrt{n(\mathbf{r}, t)}e^{i\phi(\mathbf{r}, t)}\zeta(\mathbf{r}, t) \quad (2)$$

Here, ψ is the scalar order parameter, n is the atomic density, ϕ is the scalar phase, and $\zeta = (\zeta_{+1}, \zeta_0, \zeta_{-1})^T$ is a three-component spinor quantized along the z axis, with $\zeta^\dagger \zeta = 1$. The ferromagnetic phase of the condensate (32) is the subspace obtained by all spin rotations of the spinor $\zeta_F = (1, 0, 0)_z^T$. The time evolution of the order parameter is determined by the Gross-Pitaevskii equation (see Materials and Methods).

The scalar combination $\psi = \sqrt{n}e^{i\phi}$ serves as the wave function of a quantum test charge acted upon by the synthetic electromagnetic scalar and vector potentials Φ^* and \mathbf{A}^* , which are defined by (32)

$$\Phi^* = -i\frac{\hbar}{q_e^*}\zeta^\dagger \frac{\partial}{\partial t}\zeta \quad \text{and} \quad \mathbf{A}^* = i\frac{\hbar}{q_e^*}\zeta^\dagger \nabla \zeta \quad (3)$$

where \hbar is the reduced Planck's constant. These potentials lead to the synthetic electric and magnetic fields

$$\mathbf{E}^* = -\nabla\Phi^* - \frac{\partial\mathbf{A}^*}{\partial t} \quad \text{and} \quad \mathbf{B}^* = \nabla \times \mathbf{A}^* \quad (4)$$

both of which obey Faraday's law and Gauss's law for magnetism, including the possibility of magnetic charges (25). Note that the synthetic electric charge q_e^* and the permittivity ϵ^* and permeability μ^* (appearing below) are free parameters that may be chosen to match

the values being simulated. The derivations of \mathbf{A}^* and Φ^* in the case of an initially spin-polarized sample suddenly subjected to the inhomogeneous magnetic field of Eq. 1 with $\mathbf{B}_b = 0$ are given in the Supplementary Materials. Accordingly, we focus here on the synthetic fields.

After a full spin rotation at the condensate radius R , the synthetic magnetic field is given by

$$\mathbf{B}^*(r', \theta', \varphi') = -\left(\frac{4\pi^2\hbar}{q_e^*R^2}\right) \frac{\sin^2(\pi\xi')}{(\pi\xi')^2} \times [\cos\theta' \hat{\mathbf{r}}' - \pi\xi' \sin\theta' \cot(\pi\xi')\hat{\boldsymbol{\theta}}' - \pi\xi' \sin\theta' \hat{\boldsymbol{\phi}}'] \quad (5)$$

in terms of the primed spherical coordinates (r', θ', φ') and the reduced coordinate $\xi' = r'/R$. Despite its formidable appearance, this equation has a simple interpretation in its description of \mathbf{B}^* in terms of knotted field lines, as represented in Fig. 1D. These field lines constitute a second occurrence of the Hopf fibration (33) in our Shankar skyrmion with a unit Hopf number (2). The associated synthetic electric field is

$$\mathbf{E}^*(r', \theta', \varphi') = \left(\frac{2g_F\mu_B b_q}{q_e^*}\right) \sin^2(\pi\xi') [\hat{\boldsymbol{\theta}}' - \cot(\pi\xi')\hat{\boldsymbol{\phi}}'] \sin\theta' \quad (6)$$

in terms of the Landé g -factor g_F and the Bohr magneton μ_B . These field lines lie on the surfaces of concentric spheres (Fig. 1E) and twist slightly about the polar axis in a helical sense that reverses at the radius of the skyrmion core. Note that both fields satisfy the boundary conditions $\mathbf{B}^* = 0$ and $\mathbf{E}^* = 0$ at $\xi' = 1$.

The synthetic electromagnetic fields are analytically evaluated and shown in Fig. 4 (A to D) alongside those obtained from the numerical simulations. The overall agreement is good, but there are a few minor differences between the analytic theory and the simulations that may

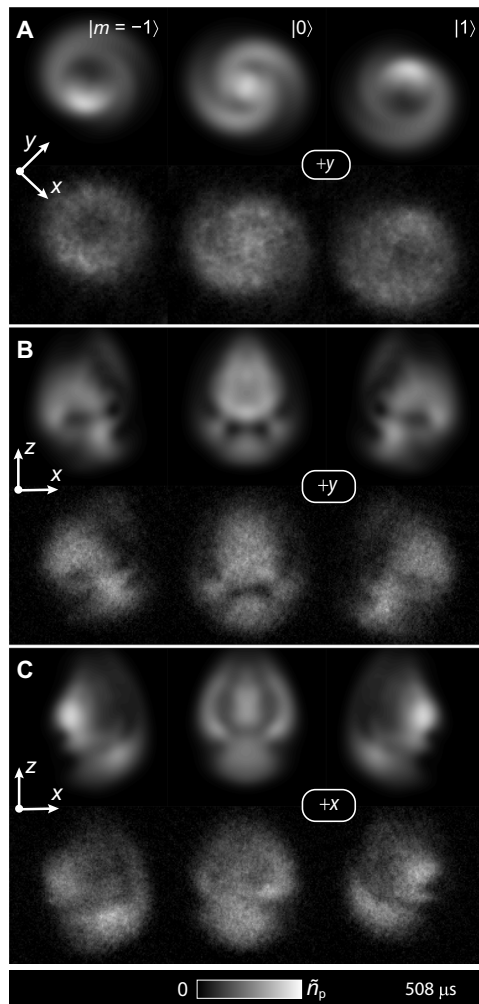


Fig. 3. Full quantum character of the skyrmion. (A) Simulated (top) and experimental (bottom) particle column densities in different spin states for 508 μs after the nonadiabatic ramp and quantization axis along $+y$. The maximum pixel intensity corresponds to column densities in excess of $\tilde{n}_p = 1.0 \times 10^9 \text{ cm}^{-2}$, and the field of view is $657 \mu\text{m} \times 438 \mu\text{m}$. (B) As in (A), but viewed from the side, with field of view $738 \mu\text{m} \times 492 \mu\text{m}$ and $\tilde{n}_p = 8.5 \times 10^8 \text{ cm}^{-2}$. (C) As in (B), but with quantization along $+x$.

be discerned in the synthetic magnetic and electric fields at the boundary of the skyrmion. These discrepancies arise as a result of the optical trapping potential and the force of the natural quadrupole magnetic field on the ferromagnetic atoms, which are not taken into account in the analytical calculations.

Maxwellian synthetic electromagnetic sources

The synthetic electromagnetic fields calculated above are not dynamical in the sense that the gauge potentials are rigidly imposed on the scalar part of the order parameter by the external control fields with no essential back action. That is, we do not implement a quantum simulation on the dynamics of the gauge fields. This feature implies that, of Maxwell's equations, only Faraday's law and Gauss's law for magnetism are required to hold. The remaining dynamics of the synthetic electromagnetic sources depends on the system we choose to simulate, in a fashion similar to the degree of freedom exercised above in choosing the value for the

synthetic permittivity and permeability. In quantum simulations of dynamical fields, however, the bosonic field responsible for synthetic electromagnetism is explicitly taken into account (20, 21), ideally fixing all relations between the synthetic electromagnetic potentials, fields, and sources. An experimental realization of such a dynamical quantum simulation remains an outstanding challenge and is beyond the scope of the present work.

We can nevertheless gain additional insight into our system by choosing to adopt the familiar Ampère's and Gauss's laws to calculate the configuration of synthetic charge and current densities that contribute to the synthetic electromagnetic fields (Eqs. 5 and 6) of a Maxwellian system. We refer below to these sources as Maxwellian synthetic charge and current densities. We stress that this choice is, in general, one of many alternatives consistent with the calculated nondynamical synthetic fields. For example, the source terms could equally respect axionic electrodynamics, which is relevant in topological insulators (35) and high-energy physics (36). In the spirit of simulation with a quantum test charge within standard classical electrodynamics, however, the assumption of Maxwellian dynamics is particularly illustrative.

The Maxwellian synthetic charge density is given by

$$\rho^*(r', \theta', \varphi') = \epsilon^* \nabla' \cdot \mathbf{E}^* = \left(\frac{4\pi\epsilon^* g_F \mu_B b_q}{q_e^* R} \right) \frac{1}{\pi \xi'} \sin^2(\pi \xi') \cos \theta' \quad (7)$$

and exhibits a dipolar character in which the net synthetic charge vanishes. The relatively lengthy expression for the Maxwellian synthetic electric current density \mathbf{J}^* is similarly derived from Maxwell's equations, as detailed in the Supplementary Materials. The field lines for \mathbf{J}^* are not themselves knotted; however, the set of points for each choice of direction of \mathbf{J}^* is found on a closed curve, and each curve is linked with all of the others to form yet another instance of the Hopf fibration. These synthetic currents correspond to the plasma streamers that sustain the ball lightning in the topological model (3).

We compare the analytical calculations and the numerical simulations of the Maxwellian sources in Fig. 4 (E to I). The agreement is good, with the most visible difference occurring in the synthetic charge density, which is depleted in the simulations in the region close to the z axis. As above, we ascribe this difference to the effects of potentials that are not considered in the analytic calculations.

DISCUSSION

Creation of the Shankar skyrmion spin texture yields simultaneous, nontrivial synthetic fields and Maxwellian sources across the extent of the condensate. As we have demonstrated, the synthetic magnetic field and Maxwellian current density are knotted and precisely match those of the topological model of ball lightning (2). The phenomena associated with ball lightning are notoriously difficult to reproduce in a laboratory setting (1), and hence, it is remarkable that our system is capable of simulating the dynamics of a quantum test charge under these conditions. More generally, the technique of tailoring spin textures through magnetic imprinting provides a rich environment for further studies of the dynamics of charged quantum matter in electromagnetic fields.

From a field-theoretical perspective, the dynamics of the Shankar skyrmion are also of interest in their own right. Although the skyrmion is topologically protected, it is also predicted to be energetically unstable against collapse to zero size (11). This question is now becoming experimentally accessible within this condensed matter system.

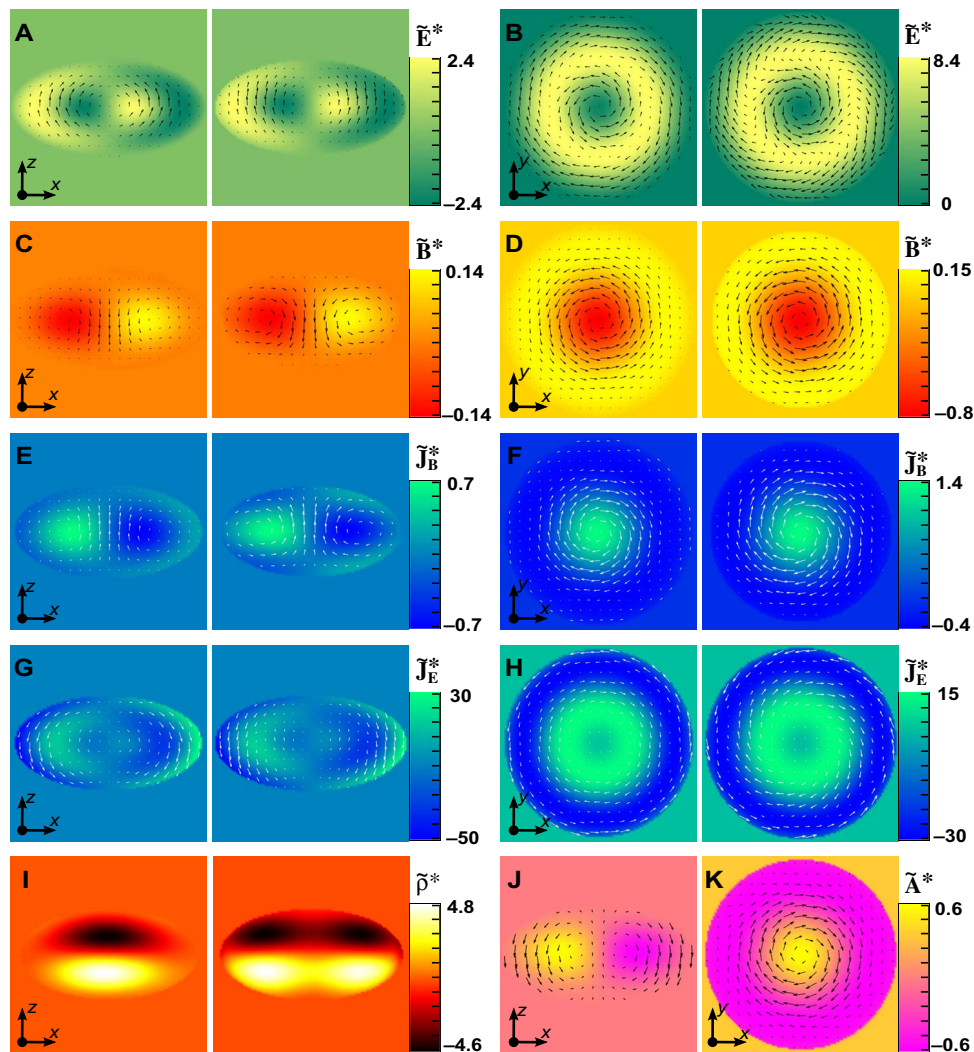


Fig. 4. Synthetic electromagnetic quantities. (A and B) Dimensionless synthetic electric field $\tilde{\mathbf{E}}^* = \frac{a_r q_E^z}{\hbar \omega_0} \mathbf{E}^*$ depicted in sections through the xz and xy planes, respectively, with the analytic result in the left half of the panel and the simulation result in the right half. The values are expressed in terms of the radial harmonic oscillator length $a_r = \sqrt{\frac{\hbar}{m\omega_0}}$. (C and D) As in (A) and (B) but for the dimensionless synthetic magnetic field $\tilde{\mathbf{B}}^* = \frac{a_r^2 q_E^z}{\hbar} \mathbf{B}^*$. (E and F) As in (A) and (B) but for the dimensionless Maxwellian synthetic electric current density associated with the synthetic magnetic field, $\tilde{\mathbf{J}}_B^* = \frac{\mu^* a_r^2 q_E^z}{\hbar} \mathbf{J}_B^*$ and (G and H) with the synthetic electric field, $\tilde{\mathbf{J}}_E^* = \frac{a_r q_E^z}{\epsilon^* \hbar \omega_0} \mathbf{J}_E^*$. (I) As in (A) but for the dimensionless Maxwellian synthetic electric charge density $\tilde{\rho}^* = \frac{a_r^2 q_E^z}{\epsilon^* \hbar \omega_0} \rho^*$. (J and K) Simulation of the dimensionless synthetic vector potential $\tilde{\mathbf{A}}^* = \frac{a_r q_E^z}{\hbar} \mathbf{A}^*$, sections in the xz and xy planes, respectively. The field of view in all panels is $13 \mu\text{m} \times 13 \mu\text{m}$. Background colors in (A), (C), (E), (G), and (I) and (B), (D), (F), (H), and (K) represent the y components and z components of the corresponding vector field, respectively. The fields and sources are evaluated $508 \mu\text{s}$ after the nonadiabatic ramp using the experimental parameters.

Our results are also related to quantum simulations of topological materials in which the winding structures arise in the momentum space. For example, a quench from a topologically trivial Hamiltonian to a topologically nontrivial one can result in the Hopf fibration for noninteracting fermions in the 2+1-dimensional momentum–time space (37). This quench is analogous to our nonadiabatic ramp of the magnetic field zero into the condensate, just as the nontrivial Hamiltonian in the topological material is analogous to the topologically nontrivial magnetic field direction on the condensate surface. Instead of tracking the temporal evolution of the system to resolve the three-dimensional topological structure (37), however, our experiment obtains an image of the skyrmion in a single shot. Nevertheless, recent advances in the measurement of the Berry curvature for ultracold fermions in driven optical

lattices pave the way toward experimental realizations of these topologically nontrivial Hamiltonians in momentum space (38).

MATERIALS AND METHODS

Experimental procedures

The experimental techniques were similar to those of Hall *et al.* (19), except that the ^{87}Rb condensate was initially prepared in the ferromagnetic phase $\zeta_F = (1, 0, 0)_z^T$. The optical trap frequencies were $\omega_r \simeq 2\pi \times 130 \text{ Hz}$ and $\omega_z \simeq 2\pi \times 170 \text{ Hz}$ in the radial and axial directions, respectively, and the total number of particles in the condensate at the moment of imaging was typically 2×10^5 . The axial Thomas-Fermi radius of the condensate was $5 \mu\text{m}$, and the corresponding radial extent was $7 \mu\text{m}$.

The bias magnetic field \mathbf{B}_b was controlled by three pairs of coils operating in the Helmholtz configuration, and the quadrupole magnetic field \mathbf{B}_q was controlled by a single pair operating in the anti-Helmholtz configuration. Initially choosing the gradient $b_q = 4.3(4)$ G/cm and the effective bias field $B_b \approx 30$ mG placed the magnetic field zero approximately 35 μm above the condensate center. During the nonadiabatic ramp, the bias field decreased to zero in approximately 10 μs . The spins precessed with a Larmor frequency $\omega_L = 2\pi \times 2.1$ kHz at the radial edge of the condensate, executing a full rotation in the Larmor time $T_L = 475$ μs . We examined the system up to times slightly beyond this to resolve the full spin rotation near the edge of the condensate.

To select a quantization axis, the magnitude of the magnetic bias field was rapidly increased along the $-x$ axis, the $+y$ axis, or the $-z$ axis, and the quadrupole magnetic field was extinguished immediately thereafter. A brief exposure to the magnetic field gradient during expansion separated the spinor components horizontally, after which they were imaged absorptively along the y and z axes in a 0.1-G field aligned with the z axis. The spinor components are labeled with respect to bases defined by the corresponding positive quantization axes.

We emphasize that the experimental images presented in this study were representative of those taken of hundreds of skyrmions over several years. Once the apparatus was calibrated, it reliably produced Shankar skyrmions on demand, apart from slight shot-to-shot fluctuations in the location of the skyrmion core.

Numerical simulations

We theoretically described the zero-temperature dynamics of the condensate using the full three-dimensional spin-1 Gross-Pitaevskii equation

$$i\hbar\partial_t\Psi(\mathbf{r}, t) = \{h(\mathbf{r}, t) + n(\mathbf{r}, t)[c_0 + c_2\mathbf{S}(\mathbf{r}, t)\cdot\mathbf{F}] - i\Gamma n^2(\mathbf{r}, t)\}\Psi(\mathbf{r}, t) \quad (8)$$

where we denote the single-particle Hamiltonian by $h(\mathbf{r}, t)$, the vector of standard spin-1 matrices by $\mathbf{F} = F_x\hat{\mathbf{x}} + F_y\hat{\mathbf{y}} + F_z\hat{\mathbf{z}}$, the spin vector by $\mathbf{S}(\mathbf{r}, t) = \zeta^\dagger(\mathbf{r}, t)\mathbf{F}\zeta(\mathbf{r}, t)$, and the density-density and spin-spin coupling constants by $c_0 = 4\pi\hbar^2(a_0 + 2a_2)/(3m)$ and $c_2 = 4\pi\hbar^2(a_2 - a_0)/(3m)$. We used the literature values for the three-body recombination rate $\Gamma = 2.9 \times \hbar \times 10^{-30}$ cm⁶/s, the ⁸⁷Rb mass $m = 1.443 \times 10^{-25}$ kg, and the s-wave scattering lengths $a_0 = 5.387$ nm and $a_2 = 5.313$ nm. The single-particle Hamiltonian assumes the form $h(\mathbf{r}, t) = -\hbar^2\nabla^2/(2m) + V_{\text{opt}}(\mathbf{r}) + g_F\mu_B\mathbf{B}(\mathbf{r}, t)\cdot\mathbf{F} + q[\mathbf{B}(\mathbf{r}, t)\cdot\mathbf{F}]^2$, where the strength of the quadratic Zeeman effect is given by $q = 2\pi\hbar \times 70$ Hz/G² and the optical trapping potential is approximated by $V_{\text{opt}}(\mathbf{r}) = \frac{m}{2}[\omega_r^2(x^2 + y^2) + \omega_z^2z^2]$. The Gross-Pitaevskii equation is integrated using a split-operator method and fast Fourier transforms on a discrete grid of 8×10^6 points. The computations were carried out using state-of-the-art graphics processing units. The simulations reproduce the experimental results with no free parameters: Only literature values for constants and independently measured parameters, such as the temporal dependence of the magnetic field, were used. The magnetic field gradient that was briefly applied to separate the different spinor components during the time-of-flight imaging was not included in the simulations.

Euler rotations and topology

The specific triad field of the Shankar skyrmion is generated by Euler axis-angle rotations $\mathcal{R}[\hat{\mathbf{r}}, wf(r)]$ of an initially uniform field with angular momentum directed along the z axis. The rotation axis $\hat{\mathbf{r}}$ is the

radial unit vector, and the rotation angle $wf(r)$ is the product of an integer topological charge w and a monotonically decreasing function of the radial distance from the origin $f(r)$, chosen such that $f(0) = 2\pi$ and $f(\infty) = 0$.

Because spin rotations in the ferromagnetic phase are isomorphic to Euler rotations, spin precession is equivalent to triad rotation about the direction of the local magnetic field \mathbf{B}_q . The rotation angles evolve at the Larmor frequency $\omega_L = g_F\mu_B b_q r'/\hbar$, expressed in primed spherical coordinates. Given $g_F = -1/2$ is negative for the ⁸⁷Rb condensate, a full -2π spin rotation at the condensate Thomas-Fermi radius R is completed at time $T_L = 2\pi\hbar/(|g_F|\mu_B b_q R)$, yielding rotation angles $\Omega(r')$ with $\Omega(0) = 0$ and $\Omega(R) = -2\pi$.

To demonstrate the topological equivalence of the spin texture at T_L to that of the Shankar skyrmion defined above, we first added a redundant 2π to $\Omega(r')$ to match it with f and continuously stretch the boundary at $r' = R$ to infinity. We then noted that the axes of the relevant Euler rotations, $\hat{\mathbf{r}}'$ and $\hat{\mathbf{B}}_q$, were related at every point by the similarity transformation $\mathcal{R}^{-1}(\hat{\mathbf{z}}', \pi)\mathcal{R}(\hat{\mathbf{B}}_q, \Omega)\mathcal{R}(\hat{\mathbf{z}}', \pi) = \mathcal{R}(-\hat{\mathbf{r}}', \Omega) = \mathcal{R}(\hat{\mathbf{r}}', -\Omega) = \mathcal{R}(\hat{\mathbf{r}}', -f)$. Because similarity transformations preserve topology, this method results in a Shankar skyrmion with a negative topological charge, $w = -1$.

As a topological entity, the skyrmionic texture was identified with an element of the third homotopy group $\pi_3(G) \cong \mathbb{Z}$, joining the quantum knot (19) as an experimental realization of a π_3 topological excitation in a quantum system.

SUPPLEMENTARY MATERIALS

Supplementary material for this article is available at <http://advances.sciencemag.org/cgi/content/full/4/3/eaao3820/DC1>

Condensate order parameter

Spin texture

Synthetic gauge potentials

Synthetic electric field

Synthetic magnetic field

Maxwellian synthetic electric charge density

Maxwellian synthetic electric current density

Superfluid velocity

fig. S1. Detailed temporal evolution of the condensate spin texture during skyrmion creation, side view, quantized along $+z$.

fig. S2. Detailed temporal evolution of the condensate spin texture during skyrmion creation, top view, quantized along $+z$.

fig. S3. Detailed temporal evolution of the condensate spin texture during skyrmion creation, side view, quantized along $+x$.

fig. S4. Detailed temporal evolution of the condensate spin texture during skyrmion creation, side view, quantized along $+y$.

fig. S5. Detailed temporal evolution of the condensate spin texture during skyrmion creation, top view, quantized along $+y$.

REFERENCES AND NOTES

1. V. L. Bychkov, A. I. Nikitin, G. C. Dijkhuys, Ball lightning investigations, in *The Atmosphere and Ionosphere, Physics of Earth and Space Environments*, V. L. Bychkov, G. V. Golubkov, A. I. Nikitin, Eds. (Springer, 2010), chap. 6, pp. 201–373.
2. A. F. Rañada, J. L. Trueba, Ball lightning an electromagnetic knot? *Nature* **383**, 32 (1996).
3. A. F. Rañada, M. Soler, J. L. Trueba, A model of ball lightning as a magnetic knot with linked streamers. *J. Geophys. Res.* **103**, 23309–23313 (1998).
4. G. E. Volovik, V. P. Mineev, Particle-like solitons in superfluid ³He phases. *Zh. Eksp. Teor. Fiz.* **73**, 767–773 (1977).
5. R. Shankar, Applications of topology to the study of ordered systems. *J. Phys. France* **38**, 1405–1412 (1977).
6. T. H. R. Skyrme, A unified field theory of mesons and baryons. *Nucl. Phys.* **31**, 556–569 (1962).
7. D. C. Wright, N. D. Mermin, Crystalline liquids: The blue phases. *Rev. Mod. Phys.* **61**, 385 (1989).

8. N. Nagaosa, Y. Tokura, Topological properties and dynamics of magnetic skyrmions. *Nat. Nanotechnol.* **8**, 899–911 (2013).
9. W. Jiang, P. Upadhyaya, W. Zhang, G. Yu, M. B. Jungfleisch, F. Y. Fradin, J. E. Pearson, Y. Tserkovnyak, K. L. Wang, O. Heinonen, S. G. E. te Velthuis, A. Hoffmann, Blowing magnetic skyrmion bubbles. *Science* **349**, 283–286 (2015).
10. U. Al Khawaja, H. T. C. Stoof, Skyrmion physics in Bose-Einstein ferromagnets. *Phys. Rev. A* **64**, 043612 (2001).
11. J. Ruostekoski, J. R. Anglin, Creating vortex rings and three-dimensional skyrmions in Bose-Einstein condensates. *Phys. Rev. Lett.* **86**, 3934 (2001).
12. L. S. Leslie, A. Hansen, K. C. Wright, B. M. Deutsch, N. P. Bigelow, Creation and detection of skyrmions in a Bose-Einstein condensate. *Phys. Rev. Lett.* **103**, 250401 (2009).
13. J.-y. Choi, W. J. Kwon, M. Lee, H. Jeong, K. An, Y.-i. Shin, Imprinting Skyrmion spin textures in spinor Bose-Einstein condensates. *New J. Phys.* **14**, 053013 (2012).
14. V. Pietilä, M. Möttönen, Creation of Dirac monopoles in spinor Bose-Einstein condensates. *Phys. Rev. Lett.* **103**, 030401 (2009).
15. M. W. Ray, E. Ruokokoski, K. Tiurev, M. Möttönen, D. S. Hall, Observation of isolated monopoles in a quantum field. *Science* **348**, 544–547 (2015).
16. E. Babaev, L. D. Faddeev, A. J. Niemi, Hidden symmetry and knot solitons in a charged two-condensate Bose system. *Phys. Rev. B* **65**, 100512 (2002).
17. E. Babaev, Dual neutral variables and knot solitons in triplet superconductors. *Phys. Rev. Lett.* **88**, 177002 (2002).
18. Y. Kawaguchi, M. Nitta, M. Ueda, Knots in a spinor Bose-Einstein condensate. *Phys. Rev. Lett.* **100**, 180403 (2008).
19. D. S. Hall, M. W. Ray, K. Tiurev, E. Ruokokoski, A. H. Gheorghe, M. Möttönen, Tying quantum knots. *Nat. Phys.* **12**, 478–483 (2016).
20. J. Dalibard, F. Gerbier, G. Juzeliūnas, P. Öhberg, *Colloquium: Artificial gauge potentials for neutral atoms*. *Rev. Mod. Phys.* **83**, 1523 (2011).
21. N. Goldman, G. Juzeliūnas, P. Öhberg, I. B. Spielman, Light-induced gauge fields for ultracold atoms. *Rep. Prog. Phys.* **77**, 126401 (2014).
22. R. P. Feynman, Simulating physics with computers. *Int. J. Theor. Phys.* **21**, 467–488 (1982).
23. Y.-J. Lin, R. L. Compton, K. Jiménez-García, W. D. Phillips, J. V. Porto, I. B. Spielman, A synthetic electric force acting on neutral atoms. *Nat. Phys.* **7**, 531–534 (2011).
24. Y.-J. Lin, R. L. Compton, K. Jiménez-García, J. V. Porto, I. B. Spielman, Synthetic magnetic fields for ultracold neutral atoms. *Nature* **462**, 628 (2009).
25. M. W. Ray, E. Ruokokoski, S. Kandel, M. Möttönen, D. S. Hall, Observation of Dirac monopoles in a synthetic magnetic field. *Nature* **505**, 657–660 (2014).
26. M. Aidesburger, M. Atala, S. Nascimbène, S. Trotzky, Y.-A. Chen, I. Bloch, Experimental realization of strong effective magnetic fields in an optical lattice. *Phys. Rev. Lett.* **107**, 255301 (2011).
27. G. Jotzu, M. Messer, R. Desbuquois, M. Lebrat, T. Uehlinger, D. Greif, T. Esslinger, Experimental realization of the topological Haldane model with ultracold fermions. *Nature* **515**, 237–240 (2014).
28. Y.-J. Lin, K. Jiménez-García, I. B. Spielman, Spin-orbit-coupled Bose-Einstein condensates. *Nature* **471**, 83–86 (2011).
29. M. C. Beeler, R. A. Williams, K. Jiménez-García, L. J. LeBlanc, A. R. Perry, I. B. Spielman, The spin Hall effect in a quantum gas. *Nature* **498**, 201–204 (2013).
30. H. Weyl, Elektron und gravitation. I. *Z. Phys.* **56**, 330–352 (1929).
31. P. A. M. Dirac, Quantised singularities in the electromagnetic field. *Proc. Royal Soc. A* **133**, 60 (1931).
32. Y. Kawaguchi, M. Ueda, Spinor Bose-Einstein condensates. *Phys. Rep.* **520**, 253 (2012).
33. H. Hopf, Über die Abbildungen der dreidimensionalen Sphäre auf die Kugelfläche. *Math. Ann.* **104**, 637–665 (1931).
34. Y. Aharonov, J. Anandan, Phase change during a cyclic quantum evolution. *Phys. Rev. Lett.* **58**, 1593 (1987).
35. X.-L. Qi, T. L. Hughes, S.-C. Zhang, Topological field theory of time-reversal invariant insulators. *Phys. Rev. B* **78**, 195424 (2008).
36. F. Wilczek, Two applications of axion electrodynamics. *Phys. Rev. Lett.* **58**, 1799 (1987).
37. C. Wang, P. Zhang, X. Chen, J. Yu, H. Zhai, Scheme to measure the topological number of a Chern insulator from quench dynamics. *Phys. Rev. Lett.* **118**, 185701 (2017).
38. N. Fläschner, B. S. Rem, M. Tarnowski, D. Vogel, D.-S. Lühmann, K. Sengstock, C. Weitenberg, Experimental reconstruction of the Berry curvature in a Floquet Bloch band. *Science* **352**, 1091–1094 (2016).

Acknowledgments

Funding: We acknowledge funding by the NSF (grant no. PHY-1519174), by the Academy of Finland (grant no. 308071) and through its Centres of Excellent Program (grant nos. 251748 and 284621), by the European Research Council (Consolidator grant no. 681311) Quantum Environment Engineering for Steered Systems (QUESS), by the Magnus Ehrnrooth Foundation, by the Education Network in Condensed Matter and Materials Physics, and by the Kaupallisten ja teknillisten tieteiden tukisäätiö (KAUTE) Foundation through its researchers abroad program. CSC-IT Center for Science Ltd. (project no. ay2090) and the Aalto Science-IT project are acknowledged for computational resources. **Author contributions:** W.L., A.H.G., and D.S.H. developed and conducted the experiments and analyzed the data. K.T. and T.O. performed the numerical simulations under the guidance of M.M. All authors discussed both experimental and theoretical results and commented on the manuscript. **Competing interests:** The authors declare that they have no competing interests. **Data and materials availability:** All data needed to evaluate the conclusions in the paper are present in the paper and/or the Supplementary Materials. Additional data related to this paper may be requested from the authors.

Submitted 20 July 2017

Accepted 23 January 2018

Published 2 March 2018

10.1126/sciadv.aao3820

Citation: W. Lee, A. H. Gheorghe, K. Tiurev, T. Ollikainen, M. Möttönen, D. S. Hall, Synthetic electromagnetic knot in a three-dimensional skyrmion. *Sci. Adv.* **4**, eaao3820 (2018).

Synthetic electromagnetic knot in a three-dimensional skyrmion

Wonjae Lee, Andrei H. Gheorghe, Konstantin Tiurev, Tuomas Ollikainen, Mikko Möttönen and David S. Hall

Sci Adv 4 (3), eaao3820.

DOI: 10.1126/sciadv.aao3820

ARTICLE TOOLS

<http://advances.sciencemag.org/content/4/3/eaao3820>

SUPPLEMENTARY MATERIALS

<http://advances.sciencemag.org/content/suppl/2018/02/26/4.3.eaao3820.DC1>

REFERENCES

This article cites 37 articles, 4 of which you can access for free
<http://advances.sciencemag.org/content/4/3/eaao3820#BIBL>

PERMISSIONS

<http://www.sciencemag.org/help/reprints-and-permissions>

Use of this article is subject to the [Terms of Service](#)

Science Advances (ISSN 2375-2548) is published by the American Association for the Advancement of Science, 1200 New York Avenue NW, Washington, DC 20005. 2017 © The Authors, some rights reserved; exclusive licensee American Association for the Advancement of Science. No claim to original U.S. Government Works. The title *Science Advances* is a registered trademark of AAAS.